Acta Materialia 119 (2016) 229–241

Contents lists available at ScienceDirect

Acta Materialia

journal homepage: www.elsevier.com/locate/actamat

Full length article

Strongly correlated breeding of high-speed dislocations

Qing-Jie Li [a], Ju Li [b, c, d, **], Zhi-Wei Shan [b, ***], Evan Ma [a, b, *]

[a] Department of Materials Science and Engineering, Johns Hopkins University, Baltimore, MD 21218, USA
[b] Center for Advancing Materials Performance from the Nanoscale (CAMP-Nano) & Hysitron Applied Research Center in China (HARCC), State Key Laboratory for Mechanical Behavior of Materials, Xi'an Jiaotong University, Xi'an 710049, PR China
[c] Department of Nuclear Science and Engineering, Massachusetts Institute of Technology, 77 Massachusetts Avenue, Cambridge, MA 02139, USA
[d] Department of Materials Science and Engineering, Massachusetts Institute of Technology, 77 Massachusetts Avenue, Cambridge, MA 02139, USA

ARTICLE INFO

Article history:
Received 1 February 2016
Received in revised form
18 June 2016
Accepted 26 July 2016
Available online 31 August 2016

Keywords:
Nanoscale single crystals
Strongly correlated plasticity
High-speed dislocations
Nanoscale metal surface

ABSTRACT

Under very high stresses, dislocations can be accelerated to approach the speed of shear wave over a distance as short as 10^1 nm. Our atomistic simulations demonstrate that dislocations with such high speeds often react in counter-intuitive manners that are beyond textbook descriptions of conventional dislocation behavior. A high-speed dislocation can "rebound" when hitting a free surface rather than simply annihilate. When two high-speed dislocations collide, they can "penetrate" through each other. An individual dislocation can even spontaneously generate multiple dislocations via self-dissociation. These anomalous mechanisms lead to rapid proliferation of dislocations that are strongly correlated both spatially and temporally, and as such may play a role in high-stress and high-strain-rate plastic deformation; a potentially related case is nanoscale pristine single crystals, which often yield via a large strain burst at ultrahigh stresses.

1. Introduction

Following the "smaller is stronger" tenet [1], a nanometer scale metallic single crystal can sustain a sample-wide stress that reaches a significant fraction of the ideal strength ($>10^{-2}$ G, where G is the shear modulus), well into the so-called ultra-strength regime [2]. In these cases, pristine samples of Au [3–5], Al [6], Fe [7], Mo and its alloy [8–10] often exhibit "instantaneous" shape change (e.g., a sudden large strain burst that collapses the sample) once the applied stress reaches the yield point. See Movie 1 through Movie 4 in Supplementary Material for a series of demonstration of the structural collapse of Al nano-pillar [6], Au nano-particle [3], Fe nano-particle [7] and Mo nano-fiber [10], respectively. This kind of cataclysmic plasticity, which is perhaps similar to the electron avalanche in strongly biased insulators during electrical breakdown, is indicative of very strong temporal correlations of a large number of mobile dislocations, but its origin remains poorly understood at present. This example highlights the need to better understand how dislocations behave and multiply, when the driving stresses are very high and the acceleration path is initially clear (obstacle free) for nucleated dislocations. The purpose of this article is to address this issue, and the mechanisms uncovered revealing highly efficient breeding of dislocations may be potentially relevant to the case mentioned above.

Supplementary video related to this article can be found at http://dx.doi.org/10.1016/j.actamat.2016.07.053.

Specifically, we describe strongly correlated plasticity via prolific dislocation multiplication mechanisms arising from dislocations running into free surfaces and into each other at very high speeds. Under an ultra-high shear stress τ, once a dislocation is nucleated, or breaks free from tangling, it may be accelerated rapidly to approach or even exceed the transverse sound speed (c_t), to become so-called "relativistic" dislocation [11] as shown by molecular dynamics (MD) simulations [12–14]. The magnitude of the relativistic acceleration length scale (l_{ra}) can be crudely

* Corresponding author. Department of Materials Science and Engineering, Johns Hopkins University, Baltimore, MD 21218, USA.
** Corresponding author. Department of Nuclear Science and Engineering and Department of Materials Science and Engineering, Massachusetts Institute of Technology, 77 Massachusetts Avenue, Cambridge, MA 02139, USA.
*** Corresponding author. Center for Advancing Materials Performance from the Nanoscale (CAMP-Nano) & Hysitron Applied Research Center in China (HARCC), State Key Laboratory for Mechanical Behavior of Materials, Xi'an Jiaotong University, Xi'an 710049, PR China.
E-mail addresses: liju@mit.edu (J. Li), zwshan@mail.xjtu.edu.cn (Z.-W. Shan), ema@jhu.edu (E. Ma).

http://dx.doi.org/10.1016/j.actamat.2016.07.053
1359-6454/

estimated by equating the work done to accelerate the dislocation, $\tau b(1-\eta)l_{ra}$, assuming a certain dissipative loss coefficient η, to the stationary energy E_0 of the dislocation as the excess energy of a relativistic dislocation could be similar to E_0 [11], which is often taken to be $E_0 = Gb^2/2$, where G is the shear modulus and b is the magnitude of Burgers vector. Since in the ultra-strength regime [2] τ is a significant fraction of the ideal strength ($>G/100$), l_{ra} will be of the order of $10^2 b$, or 10^1 nm (see Fig. S1 and associated discussion in online Supplementary Material for the estimation of dissipation coefficient and the acceleration length). A distance of this magnitude for dislocations to accelerate, free of obstacles, is easily available for the first batch of dislocations, after they nucleate from the surface of a pristine nanoscale crystal that often yield at ultrahigh stresses.

Once a high speed of the order of c_t is reached, the stress field, energy, etc. of a dislocation become significantly modified due to the "relativistic" or inertia effects [11,15–19]. Thereupon, anomalous dislocation behaviors and reactions may emerge. In the following, we use MD simulations to systematically illustrate the spectrum of unconventional reactions of high-speed dislocations. We will also briefly comment on their implications on extremely transient but large-amplitude plasticity, for example that seen in nanometer scale pristine single crystals.

2. Simulation methods

A model material based on an empirical potential for Cu [20] was chosen for the current study as an example. This empirical potential of Cu has been successfully applied to a wide range of simulations, including those involving dislocations under high stresses [21–23]. Parallel simulations were performed on Al [24–27], Ni [24] and Au [28] as well, to ensure that the observed phenomena are general and not restricted to a specific metal or a particular interatomic potential. Specifically, we focused on the reactions when a high-speed dislocation hits free surface or other dislocations.

In all our simulations on interactions between high-speed dislocations and free surface or other high-speed dislocations, the samples were first equilibrated under constant stress using Parrinello-Rahman method [29] with an initial temperature that was not controlled by any thermostats thereafter due to the non-equilibrium nature of high-speed dislocation dynamics (a global Nose-Hoover thermostat was also tested and showed negligible difference compared to the results reported here). Initial temperatures ranging from 2 to 400 K were tested to ensure finite temperature has minor effects on the observed high-speed dislocation behaviors (the results with initial temperature of 2 K are shown in the current work). Following the equilibration, a dislocation was introduced from the crystal surface and accelerated by the applied constant stress. Periodic boundary conditions were employed along the dislocation line direction. While some MD simulations on dislocation dynamics also used periodic boundary conditions in the direction of dislocation motion to extend the gliding distance, here we purposely set up free surface in this direction, as free surfaces are generally the terminus of dislocations in nanoscale single crystal metals. The atomistic configurations of dislocations were identified by the common neighbor analysis [30,31] and the dislocation extraction algorithm [32] and visualized using AtomEye [33]. Dislocation speeds were computed by identifying the dislocation positions at different time. All dislocation speeds used are the instantaneous speeds right before dislocation reactions. A time step of 1 fs was used throughout all simulations which were carried out with the LAMMPS package [34]. Further details on the MD simulations can be found in Supplementary Material.

3. Results and discussion

3.1. Speed-dependent reactions of dislocation with free surface

Interfaces such as grain boundaries, phase boundaries has been extensively studied as they often play an important role in materials' mechanical properties via dislocation-interface interactions. However, when materials scale down to nanometer dimensions and become single crystals that are free of pre-existing dislocations, dislocation-free surface interactions have been largely overlooked as one often expects that dislocation should simply annihilate at free surfaces, as shown in Fig. 1(a): here a relatively slowly moving (instantaneous speed before annihilation is $v \sim 0.56c_t$, where $c_t = 2920$ m/s is the shear wave speed) screw dislocation (screw dislocations are thought to be easily nucleated than edge or mixed dislocation in nanoscale single crystals [22,35]) simply annihilates at the free surface of a slab configuration which is subject to a shear stress of 0.4 GPa and an initial temperature of 2 K. This annihilation process reduces the number of active dislocations (n_d) from 1 to 0, as often discussed in the dislocation starvation model [36]. However, when the dislocation speed becomes sufficiently high, the incident dislocation often does not simply disappear. Instead, it can "bounce back" from the free surface. As shown in Fig. 1(b), when the instantaneous speed before hitting a surface is increased to $v \sim 0.66c_t$ (by applying a higher shear stress 1.0 GPa), a new partial dislocation is immediately generated (31.0 ps) and accelerated to glide back (40.0 ps) upon its annihilation at free surface (25.0 ps–28.0 ps). This annihilation-regeneration process, which occurs within only a few picoseconds, appears as if the incident dislocation partially rebounded from the free surface. As a result, n_d is kept constant after the reaction ($1 \rightarrow 1$). Additionally, a small atomic step was created on the surface as the rebounded partial dislocation is of mixed character. Also due to the stacking fault ribbon of the incident dislocation, the rebounded partial dislocation (with opposite Burgers vector as to the leading partial of the incident dislocation) generally does not appear on exactly the same slip plane (otherwise atoms on the two oppositely shifted atomic planes will sit on top of each other) as that of the incident dislocation but appear one slip plane above. If the speed further approaches c_t, an incident dislocation could even rebound into multiple new dislocations. As shown in Fig. 1(c), for instantaneous speed $v \sim 0.78c_t$ (the applied shear stress now is 1.8 GPa) before hitting a surface, the dislocation core becomes wider (the dislocation now enters the so-called "breathing mode" [37–39] in which the separation between leading and trailing partials varies quasi-periodically in time) before hitting free surface such that the leading partial and trailing partial are obviously separated and rebound one after the other. The leading partial first rebounds into a new partial dislocation, before the trailing partial hits the free surface (22.6 ps). Then the trailing partial hits the free surface and annihilates (24.4 ps), upon which three new partials are immediately generated (27.0 ps). One of them is a trailing partial that complements the first rebounded partial to form a full dislocation, and the other two are leading partials running on other neighboring slip planes. Consequently, n_d is tripled after the reaction ($1 \rightarrow 3$).

For convenience, we use the following convention to name the rebound events: $b^{reb}/b^{inc}<1 \rightarrow$ partial-rebound, $b^{reb}/b^{inc} = 1 \rightarrow$ full-rebound, $n_d^{reb}/n_d^{inc} = 1 \rightarrow$ single rebound, $n_d^{reb}/n_d^{inc} = 2 \rightarrow$ double rebound and $n_d^{reb}/n_d^{inc} \geq 3 \rightarrow$ multiple rebound, where b^{reb} and b^{inc} are the magnitude of Burgers vectors of rebounding and incident dislocations, and n_d^{reb} and n_d^{inc} are the number of rebounded dislocations and the number of incident dislocations, respectively. Such a scheme is also used to describe other reactions that will be discussed later. More detailed illustrations about the above

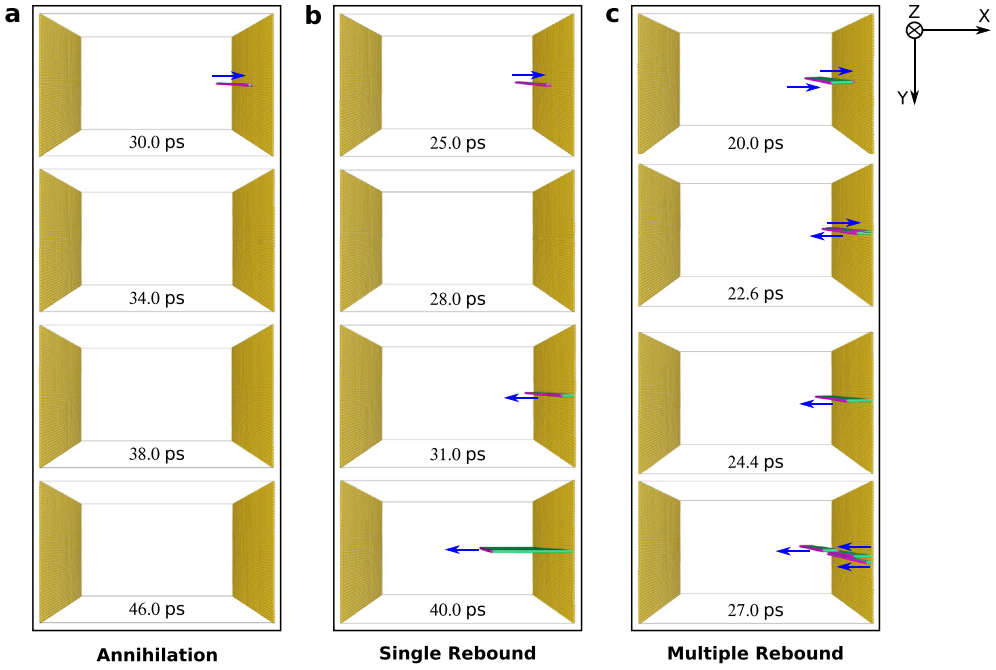

Fig. 1. With increasing dislocation speed, full screw dislocation experiences annihilation, single rebound and multiple rebound at free surface. (a) Simple annihilation at an instantaneous incident speed $v \sim 0.56c_t$ (also see Movie 5 in Supplementary Material) under the shear stress of 0.4 GPa. (b) Rebounding into a single partial dislocation at a higher instantaneous incident speed $v \sim 0.66c_t$ under the shear stress of 1.0 GPa (also see Movie 6 in Supplementary Material). (c) Rebounding into a full screw dislocation and two partial dislocations at an even higher instantaneous incident speed $v \sim 0.78c_t$ under the shear stress of 1.8 GPa (also see Movie 7 in Supplementary Material). c_t is the transverse sound speed (2920 m/s for Cu in this work). *X*, *Y* and *Z* are along $[11\bar{2}]$, [111] and $[1\bar{1}\,0]$, respectively. Atoms on free surfaces, dislocation cores and stacking faults are rendered in yellow, magenta and green color, respectively. The short blue arrows indicate the direction of dislocation motion.

annihilation, single partial-rebound and multiple partial-rebound scenarios can be seen in Movie 5 through Movie 7 in Supplementary Material. Note that in all these simulations anomalous dislocation rebounds take place in a shear stress range of 0.6–1.8 GPa, or 10^{-2} *G*, which is a stress level typically observed in experiments on nanoscale samples [6,9,10,40–43].

Supplementary video related to this article can be found at http://dx.doi.org/10.1016/j.actamat.2016.07.053.

In nanoscale single crystals, often the surface nucleated dislocation is a leading partial dislocation [40–42,44,45], which runs across the crystal and hits the opposite sample surface before a trailing partial appears. We therefore examine the reaction of a single incident partial dislocation at the free surface. As shown in Fig. 2(a) (also see Movie 8 in Supplementary Material), a 30° partial dislocation annihilates at the free surface even though its instantaneous incident speed is already as high as $v \sim 0.88c_t$ (the applied shear stress is 1.2 GPa). This partial dislocation annihilation occurs over a wide speed range, which will be rationalized later. When the instantaneous speed before hitting a surface is very close to c_t, as shown in Fig. 2(b) ($v \sim 0.97c_t$ and applied shear stress is 1.6 GPa, also see Movie 9 in Supplementary Material), the incident partial dislocation does rebound into two partials on neighboring slip

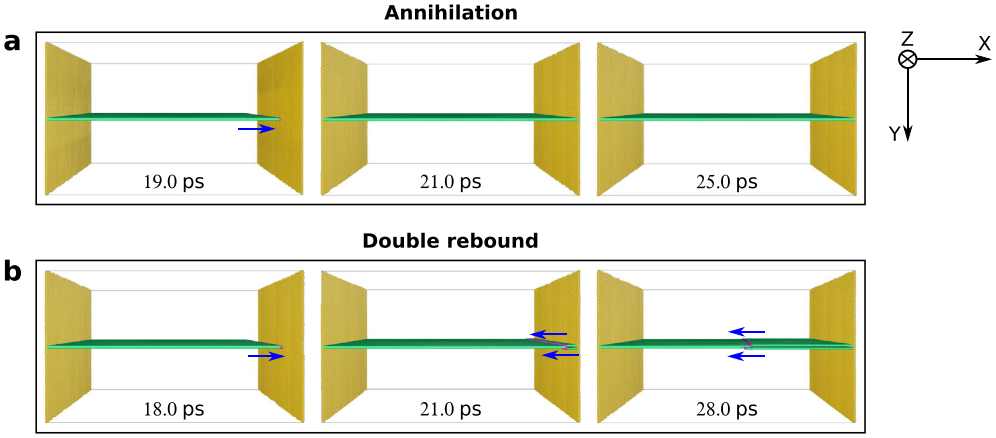

Fig. 2. A 30° partial dislocation experiencing annihilation and double rebound at free surface with increasing speed. (a) A 30° partial dislocation simply annihilates at the free surface with an instantaneous incident speed $v \sim 0.88c_t$ under the applied shear stress 1.2 GPa (also see Movie 8 in Supplementary Material). (b) Under the applied shear stress 1.6 GPa, a 30° partial dislocation rebounds into two partial dislocations on neighboring slip planes at a higher instantaneous incident speed $v \sim 0.97c_t$ (also see Movie 9 in Supplementary Material). $c_t = 2920$ m/s is the transverse sound speed. *X*, *Y* and *Z* are along $[1\bar{1}\,0]$, [111] and $[\bar{1}\,1\,2]$, respectively. Atoms on free surfaces, dislocation cores and stacking faults are rendered in yellow, magenta and green color, respectively. The short blue arrows indicate the direction of dislocation motion.

planes, forming a nucleus for a subsequent deformation twin. Similar behaviors are also found for 60° partial dislocations except that the critical speed needed for rebound is even higher (see Fig. S2 in Supplementary Material).

Supplementary video related to this article can be found at http://dx.doi.org/10.1016/j.actamat.2016.07.053.

The behavior of edge dislocations are examined next. They are found to show even more possibilities, because an edge dislocation can have a speed v not only in the subsonic regime ($v < c_t$), but also in the transonic ($c_t < v < c_l$, where c_l is the longitudinal wave speed) regime [12]. As shown in Fig. 3, a slab setup (periodic boundary conditions in x and z directions) is used: an edge dislocation would glide toward the free surfaces under an uniaxial tensile or compressive stress (applied along x direction). Fig. 3 shows the reactions under different *compressive* stresses. In the subsonic speed regime, an edge dislocation also experiences transitions from simple annihilation to single partial-rebound to multiple partial-rebound, similar to those discussed above for screw dislocations. For example, in Fig. 3(a), an edge dislocation with the instantaneous incident speed $v \sim 0.58c_t$ (applied axial stress is 2.0 GPa) simply annihilates at free surface. However, as shown in Fig. 3(b), an edge dislocation running at a higher instantaneous incident speed

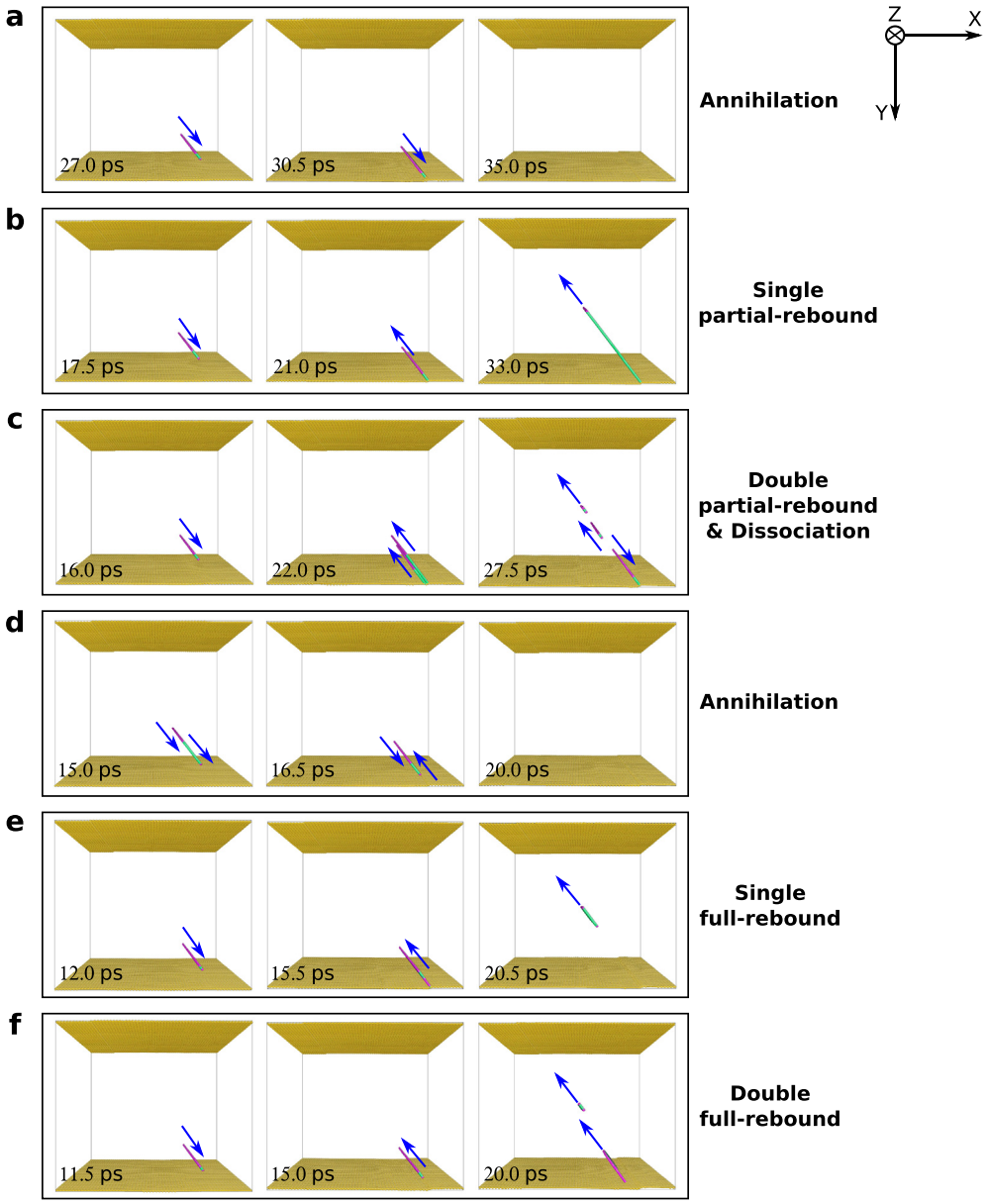

Fig. 3. Full edge dislocation-free surface interactions at different dislocation speeds under compressive axial stress. (a–c) Interaction between free surface and a subsonic edge dislocation. (d–f) Interaction between free surface and a transonic edge dislocation. (a) A full edge dislocation with speed $v \sim 0.58c_t$ ($0.33c_l$) at axial stress 2.0 GPa annihilates at free. (b) A full edge dislocation rebounds into a single partial dislocation at a higher incident speed $v \sim 0.91c_t$ ($0.51c_l$) under the axial stress of 3.2 GPa. (c) At an even higher instantaneous incident speed $v \sim 1.00c_t$ ($0.56c_l$) under the axial stress of 5.2 GPa, a full edge dislocation rebounds into two partial dislocations which further transformed into two full dislocations via the dissociation of stacking faults. (d) A full edge dislocation with an instantaneous incident speed $v \sim 1.10c_t$ ($0.62c_l$, the axial stress is 5.6 GPa) annihilates at free surface by rebounding the leading partial into a trailing partial which then annihilates with the incident opposite trailing partial. (e) A full edge dislocation with an instantaneous incident speed $v \sim 1.35c_t$ ($0.76c_l$, the applied axial stress is 7.2 GPa) directly rebounds into a full dislocation. (f) At an even higher instantaneous incident speed $v \sim 1.36c_t$ ($0.77c_l$, the applied axial stress is 8.0 GPa), a full edge dislocation rebounds into two full dislocations directly. $c_t = 2920$ m/s and $c_l = 5182$ m/s are the transverse and longitudinal sound speeds, respectively. X, Y and Z are along [201], $[1\bar{5}\bar{2}]$ and $[11\bar{2}]$, respectively. Atoms on free surfaces, dislocation cores and stacking faults are rendered in yellow, magenta and green color, respectively. The short blue arrows indicate the direction of dislocation motion.

$v \sim 0.91c_t$ rebounds into a single partial dislocation (the applied axial stress is 3.2 GPa). At still higher instantaneous incident speed as shown in Fig. 3(c) ($v \sim 1.0c_t$ at the axial stress of 5.2 GPa), the incident dislocation rebounds into two leading partials on different slip planes. Then the stacking faults created in the wake of these two leading partials become unstable and dissociate into trailing partials which eliminate the stacking faults and form full dislocations with the leading partials (27.5 ps). This behavior extends into the transonic speed regime. For example, at an instantaneous incident speed such as $v \sim 1.1c_t$ (equal to $0.62c_l$, where c_l is the longitudinal sound velocity) (Fig. 3(d), the applied axial stress is 5.6 GPa), the incident full edge dislocation (composed of leading partial and trailing partial) annihilates via reactions involving rebound partials: the leading partial rebounds into a trailing partial, which then simply annihilates with the incident trailing partial (of opposite sign). Different from the subsonic speed regime, the incident edge dislocation in transonic speed regime can also directly rebound into one (Fig. 3(e)) or two (Fig. 3(f)) full dislocations provided that the instantaneous incident speed is high enough, e.g., $v \sim 1.35c_t$ (the applied axial stress is 7.2 GPa) and $v \sim 1.36c_t$ (the applied axial stress is 8.0 GPa) in Fig. 3(e) and (f), respectively.

When the loading stress was changed to *tensile* for the above setup of edge dislocation, rebound only occurs in the transonic speed regime, via separate and sequential rebounding of the leading partial and the trailing partial (see Fig. 4(b)). However, with high enough instantaneous incident speeds such as $v \sim 1.21c_t$ (the corresponding instantaneous speed of trailing partial is $v_t \sim 0.97c_t$), the trailing partial usually dissociates into three ($\mathbf{b} \rightarrow 2\mathbf{b} - \mathbf{b}$, preserving a constant net Burgers vector) partials before they hit free surface and rebound (see Fig. 4(c)), significantly increasing n_d. Such a self-dissociation phenomenon is consistent with previous hypothesis [46] and MD simulation [47].

The above sharp transition from simple annihilation to rebound at free surface when the applied stress and dislocation speed exceed a critical value turns out to be a general phenomenon. First of all, this transition has been widely observed in many other metals modeled by different empirical potentials. For example, Fig. S3 in Supplementary Material shows the surface rebound of a screw dislocation in Al [24], Au [28] and Ni [24], respectively. Second, the annihilation→rebound transition has been observed for different type of dislocations as demonstrated above. Last but not least, the annihilation→rebound transition occurs over a wide range of temperatures from 2 K to >400 K (see Fig. S4 in Supplementary Material for an example of surface rebound at the initial temperature of 300 K), indicating that finite temperature dependent energy dissipation has minor effects on surface rebound process (the temperature rise due to energy dissipation is usually around several kelvin).

3.2. Energy – Burgers vector criterion

We now rationalize the observed sharp annihilation→rebound transition. According to Frank's rule, two dislocations with Burgers vectors $\mathbf{b}_1$ and $\mathbf{b}_2$ can react to form a new dislocation with Burgers vector $\mathbf{b}_3 = \mathbf{b}_1 + \mathbf{b}_2$ as long as $|\mathbf{b}_3|^2 < |\mathbf{b}_1|^2 + |\mathbf{b}_2|^2$. This is based on the notion that the potential energy per unit length of a dislocation can be approximated as $\alpha G b^2$, where α is a constant, G is shear modulus and b is the magnitude of Burgers vector. Potential energy excess from a dislocation reaction is converted into heat, E_{incoh}, i.e.,

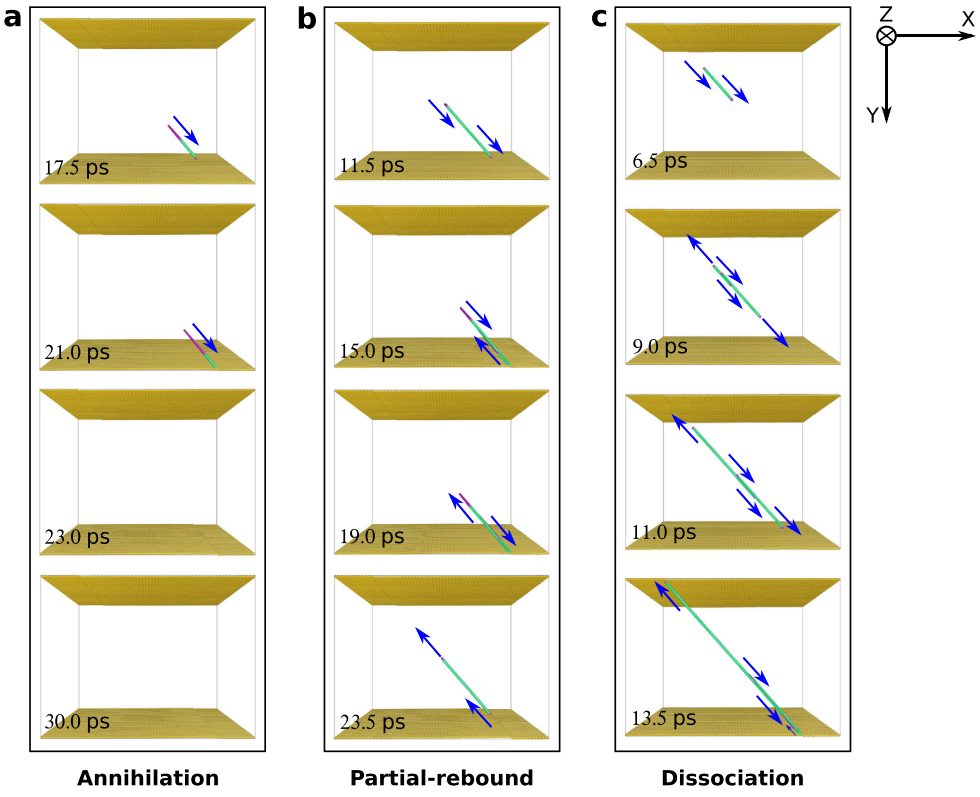

Fig. 4. Full edge dislocation-free surface reactions under tensile axial stress. (a) With an instantaneous incident speed $v \sim 0.91c_t$ (the applied axial stress is 2.0 GPa), a full edge dislocation just simply annihilates at the bottom free surface. (b) At a higher instantaneous incident speed $v \sim 1.15c_t$ (the applied axial stress is 3.2 GPa), the incident leading and trailing partials rebound into a new pair of leading and trailing partials, separately and sequentially. (c) With an even higher instantaneous incident speed such as $v \sim 1.21c_t$ (the applied axial stress is 3.6 GPa), the trailing partial spontaneously dissociates into three partial dislocations. Two of them have the same Burgers vector while the other one has opposite Burgers vector. *X*, *Y* and *Z* are along [201], [$1\bar{5}\bar{2}$] and [$11\bar{2}$], respectively. Blue arrows indicate the motion directions of dislocations.

the incoherent kinetic energies of the atoms. However, for high-speed dislocations, the coherent *kinetic* energy K can be as important as the stationary potential energy E_0.

An atomistic system near equilibrium would have its total excitation energy E nearly uniformly distributed among its $3N$ degrees of freedom, where N is the number of atoms. But, for a system far from equilibrium, i.e., with high-speed dislocations in this case, certain "modes" could gain disproportionally large potential and kinetic energies amongst the $3N$ modes. We can therefore decompose E into the coherent energy of these few soliton-like modes E_{coh}, plus the rest, which is randomized incoherent energy or heat E_{incoh}. The energy from external work is injected into the soliton-like coherent modes first, which then dissipate to the rest of the modes:

$$\frac{dE_{\mathrm{coh}}}{dt} = \sum_{i=1}^{M} b\sigma_i \frac{dx_i}{dt} - \frac{dE_{\mathrm{incoh}}}{dt}, \quad \frac{dE_{\mathrm{incoh}}}{dt} = \sum_{i=1}^{M} D_i, \tag{1}$$

where the index i runs over the M dislocations in the system. The dissipation kernel D_i takes the form of radiative loss and phonon drag when the dislocations are translating, and depends on both the dislocation speeds and phonon temperature: $D_i = D_i \ (E_{\mathrm{coh}}, E_{\mathrm{incoh}})$. The coherent energy of the soliton-like modes consists of the potential and kinetic energy of dislocations in the system, i.e., $E_{\mathrm{coh}} = \sum_{i=1}^{M}(P_i + K_i)$, where P_i and K_i are the potential energy and kinetic energy of dislocation i moving at speed v_i, respectively. According to the relativistic dislocation mechanics [11] for screw dislocation, $P_i = E_{0,i}(1 - v_i^2/(2c_t^2))/(1 - v_i^2/c_t^2)^{1/2}$, $K_i = E_{0,i}(v_i^2/c_t^2)/(2(1 - v_i^2/c_t^2)^{1/2})$. For an assembly of reactant dislocations $\{\mathbf{b}_i, E_{\mathrm{coh},i}\}$ that react to form products $\{\mathbf{b}_j, E_{\mathrm{coh},j}\}$, there is generally

$$\sum_{\text{reactants}} \mathbf{b}_i = \sum_{\text{products}} \mathbf{b}_j \tag{2}$$

and loss of coherent energy:

$$\sum_{\text{reactants}} E_{\mathrm{coh},i} > \sum_{\text{products}} E_{\mathrm{coh},j} \tag{3}$$

Note that Equation (2), which is conservation of geometric incompatibilities in an elastic medium, can be violated near free surfaces, due to adjacency to zero-modulus vacuum. (3) is an inequality that must be satisfied at all points of the reaction. However we discover that most anomalous reactions occur only if

$$\sum_{\text{reactants}} K_i \gtrsim \sum_{\text{products}} E_{0,j} - E_0^{\mathrm{LI}} \tag{4}$$

a stronger condition than (3), as illustrated in Fig. 5, where E_0^{LI} is the lowest potential energy intermediate (LI) state. (If $\sum_{\text{reactants}} \mathbf{b}_i = 0$ or if the reaction involves annihilation near surface, the lowest intermediate state is just dislocation-free crystal and E_0^{LI} is zero.) This is because most of the excess reactant potential energy are dissipated first into heat when they reached the intermediate state, and are not useful for subsequent abnormal leg of the reaction.

In the following, we verify the underlying mechanism in term of the criteria discussed above for the various abnormal dislocation behaviors, first qualitatively, and then quantitatively. To this end, we first carried out two sets of simulations that involve reactions between two co-planar opposite-sign dislocations, and reactions between two non-coplanar partial dislocations. First, let us consider the coplanar opposite dislocation reactions. As shown in Fig. 6, when approaching each other with lower incident speeds (Fig. 6(a)), two opposite full screw dislocations on the same slip plane simply annihilates, as expected from the textbook prediction.

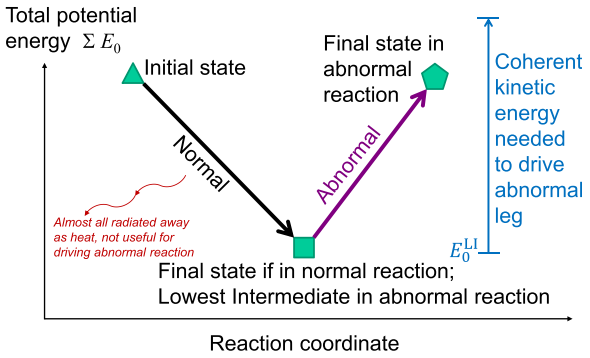

Fig. 5. Illustration of abnormal dislocation-reaction pathway. Reaction starts at an initial state (the triangle in figure) with higher potential energy and then proceeds toward a lower potential energy state (the square in figure), as suggested by Frank's rule. The excess potential energy of this step almost radiates away as heat. This is the final state of normal dislocation reactions but the lowest potential energy intermediate (LI) state for abnormal reactions of high speed dislocations, as the coherent *kinetic* energies carried by high-speed dislocations could drive the LI state to a new higher potential energy state (the pentagon in the figure).

However, upon collision at higher incident speeds (Fig. 6(b), also see Movie 10 in Supplementary Material), two opposite coplanar partial dislocations are immediately created and accelerated to glide in opposite directions, looking as if the incident dislocations had partially "penetrated" through each other. At even higher collision speeds (Fig. 6(c), also see Movie 11 in Supplementary Material), the incident dislocations not only fully "penetrate" each other but also create additional partial dislocations on an intersecting slip plane, leading to an "explosion" in dislocation number n_{d}. This generation of new dislocations on a secondary slip plane is not unique for two opposite dislocations colliding into each other but was also observed for dislocations impacting on free surface. Similar reactions are also observed for other type of dislocations such as full edge dislocation, 30° partial dislocation and 60°partial dislocation (see Figs. S5–S7 in Supplementary Material, respectively). The above results are consistent with our equation (4) criteria, as the reactions can be expressed as: $\mathbf{b} + (-\mathbf{b}) + 2K \rightarrow 0 + 2K \rightarrow \mathbf{b}_{\mathrm{p}} + (-\mathbf{b}_{\mathrm{p}})$, and $\mathbf{b} + (-\mathbf{b}) + 2K \rightarrow 0 + 2K \rightarrow \mathbf{b} + (-\mathbf{b}) + \mathbf{b}_{\mathrm{p}} + (-\mathbf{b}_{\mathrm{p}})$, where K is the kinetic energy of a single moving dislocation, and $\mathbf{b}_{\mathrm{p}}$ is the Burgers vector of partial dislocation. Similar reactions of coplanar dislocations were also reported for a body centered cubic metal Nb [48].

Supplementary video related to this article can be found at http://dx.doi.org/10.1016/j.actamat.2016.07.053.

Fig. 7 shows the reactions between two partial dislocations that glide on two different but intersecting planes, i.e., the left partial dislocation with Burgers vector [211]/6 gliding on $(\bar{1}11)$ and the right partial dislocation with Burgers vector $[\bar{2}11]/6$ gliding on (111) plane. Under tensile stresses along x direction, both of them glide towards the free surface on the bottom. As designed, the two partial dislocations glide into each other and form a Lomer-Cottrell (LC) dislocation configuration when the incident speeds are low (e.g., $v_1 \sim 0.68c_t$ and $v_2 \sim 0.62c_t$ under an applied tensile axial stress 1.0 GPa in Fig. 7(a)); this is the normal L-C lock formation mechanism well known in the literature (also see Movie 12 in Supplementary Material). But when the instantaneous incident speeds increase to a higher level such as $v_1 \sim 0.74c_t$ and $v_2 \sim 0.73c_t$ under an applied tensile axial stress 1.7 GPa (Fig. 7(b), also see Movie 13 in Supplementary Material), one partial dislocation is immediately emitted upon the formation of the LC dislocation while the other reactant partial is simply blocked at the stacking fault. This leads to half "penetration". At even higher instantaneous incident speeds such as $v_1 \sim 1.69c_t$ and $v_2 \sim 1.70c_t$ under an applied tensile axial

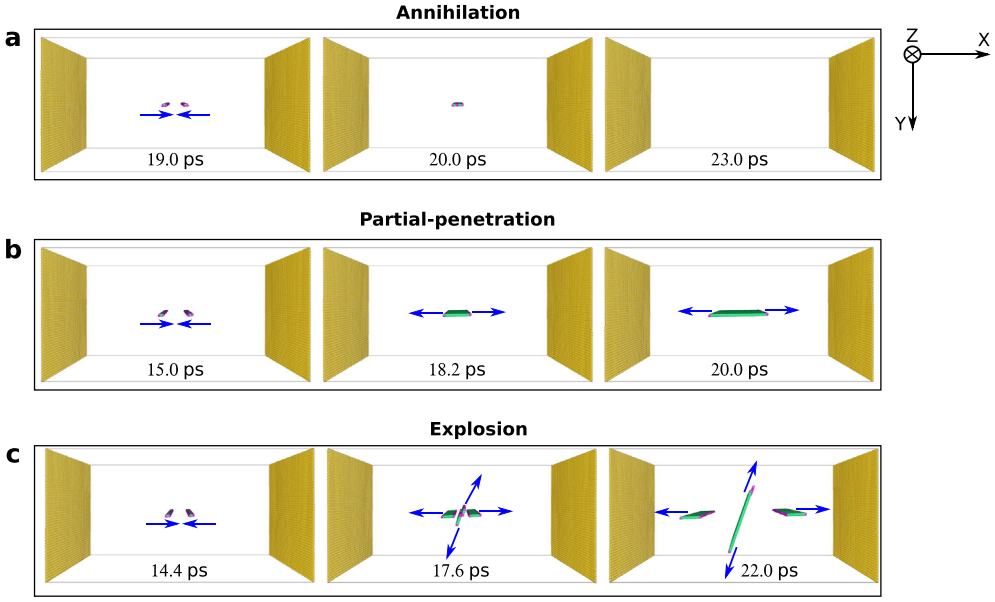

Fig. 6. Two coplanar opposite full screw dislocations experiencing annihilation, partial-penetration and full penetration at increasing speeds. The left dislocation is denoted as dislocation 1 and the right dislocation is denoted as dislocation 2. (a) The two colliding dislocations annihilate with the instantaneous incident speeds $v_1 \sim 0.57c_t$ and $v_2 \sim 0.57c_t$ under the applied shear stress 0.4 GPa. (b) At higher instantaneous incident speeds $v_1 \sim 0.66c_t$ and $v_2 \sim 0.66c_t$ under applied shear stress 1.2 GPa, they partially penetrate each other (also see Movie 10 in Supplementary Material). (c) At significantly higher instantaneous incident speeds $v_1 \sim 0.68c_t$ and $v_2 \sim 0.77c_t$ under applied shear stress 1.6 GPa, they fully penetrate through each other, accompanied by an explosive generation of dislocations on nearby planes (also see Movie 11 in Supplementary Material). $c_t = 2920$ m/s is the transverse sound speed. *X*, *Y* and *Z* are along $[11\bar{2}]$, [111] and $[1\bar{1}\,0]$, respectively. Atoms on free surfaces, dislocation cores and stacking faults are rendered in yellow, magenta and green color, respectively. The short blue arrows indicate the direction of dislocation motion.

stress 2.5 GPa (Fig. 7(c), also see Movie 14 in Supplementary Material), the two incident partials first form a LC dislocation which then immediately dissociates into two new partial dislocations, leading to a full "penetration". These processes can be described by the following reactions: $\mathbf{b}_{p1} + \mathbf{b}_{p2} + 2K \rightarrow \mathbf{b}_{LC} + 2K \rightarrow \mathbf{b}_{p1}$, and $\mathbf{b}_{p1} + \mathbf{b}_{p2} + 2K \rightarrow \mathbf{b}_{LC} + 2K \rightarrow \mathbf{b}_{p1} + \mathbf{b}_{p2}$, where the $\mathbf{b}_{LC}$ state in the middle equations is the LI state.

Supplementary video related to this article can be found at http://dx.doi.org/10.1016/j.actamat.2016.07.053.

Note that the free surface rebound behavior discussed earlier can also be rationalized by a similar reaction: $\mathbf{b} + \mathbf{b}_{im} + 2K \rightarrow 0 + 2K \rightarrow \sum_{products} \mathbf{b}_j^{reb} + \mathbf{b}_{im,j}^{reb}$, where $\mathbf{b}_{im} = -\mathbf{b}$ is the image dislocation Burgers vector, $\mathbf{b}_j^{reb}$ is the Burgers vector of the *j*th rebounded dislocation. The re-birth of new dislocations from the excess kinetic energy is akin to the creation of elementary particles in high-energy physics, where once a certain energy threshold is reached, new charged particles could be created out of "vacuum". Here dislocations are created in several unconventional ways, multiplying in number rapidly. These "rebound" and "penetration" behaviors are consistent with the predictions in 1948 by F.C. Frank, who hypothesized that relativistic dislocation-surface interactions could become a dislocation source mechanism [49]. It should be emphasized that the kinetic energy effects discussed here are fundamentally different from the various dislocation reactions at surfaces previously discussed [50–52]. In those cases, although the hypothesized reactions also provide dislocations that are different from incident dislocations, they are solely based on Frank's rule, in the conventional realm of potential-energy-controlled dislocation reactions.

More quantitatively, for screw dislocations, equation (4) is

$$\sum_{\text{reactants}} \frac{E_{0,i}}{2}\left(v_i^2/c_t^2\right)\left(1 - v_i^2/c_t^2\right)^{-1/2} = \sum_{\text{products}} E_{0,j} \qquad (5)$$

From equation (5), the critical speed of screw dislocations could be roughly estimated. For example, when a screw dislocation is partially rebounded or partially penetrates an opposite dislocation, $E_0/2(v^2/c_t^2)(1 - v^2/c_t^2)^{-1/2} \sim 1/4E_0$, assuming the rest energy of a partial dislocation is 1/2 of that of a full dislocation (a full dislocation can be considered as a combination of leading and trailing partial dislocations provided that the dissociation width is small) and a dislocation close to surface or opposite dislocation only has 1/2 of the rest energy of a dislocation far from surface or an opposite dislocation. This leads to a critical speed $v_p = 0.625c_t$ for partial rebound or partial penetration. This estimate is close to our MD simulation results which suggest critical speeds $v \sim 0.57c_t$ and $v \sim 0.66c_t$ (both are the instantaneous speeds right before the reactions) for a full screw dislocation rebounding into a partial dislocation or partially penetrating an opposite full screw dislocation, respectively. To ascertain that our results are not restricted to a specific metal or a particular potential, we also made comparisons for Au [28] and Ni [24]. For single partial rebound, our MD simulations suggested critical speeds ~$0.65c_t$ and ~$0.65c_t$ (both are instantaneous speeds before rebound) for Au and Ni, respectively.

Special attention should be paid to partial dislocations. Due to the symmetry of FCC crystal structure, partial dislocations usually suffer from the $\mathbf{b}_p \leftrightarrow -\mathbf{b}_p$ asymmetry on a specific slip plane such that a leading partial dislocation $\mathbf{b}_p$ cannot rebound into an opposite partial dislocation $-\mathbf{b}_p$ on exactly the same slip plane. Instead, it often attempts to rebound into opposite partial dislocations (with Burgers vector $-\mathbf{b}_p$) on the neighboring slip planes. Accordingly, the total kinetic energy $\sum_{i=1}^{M} K_i$ is partitioned into two parts, each for one side of the incident slip plane. For screw dislocations under simple shear (as shown in Fig. 2), the partition coefficient could simply be ~0.5 because both sides of the incident slip plane are virtually equivalent. Because of this partitioning of kinetic energy, the minimum critical speed for rebound is increased; a double rebound has to be initiated in lieu of a single rebound. For example, estimation made based on equation (5) for a partial screw dislocation rebounding or penetrating into two new partials gives a

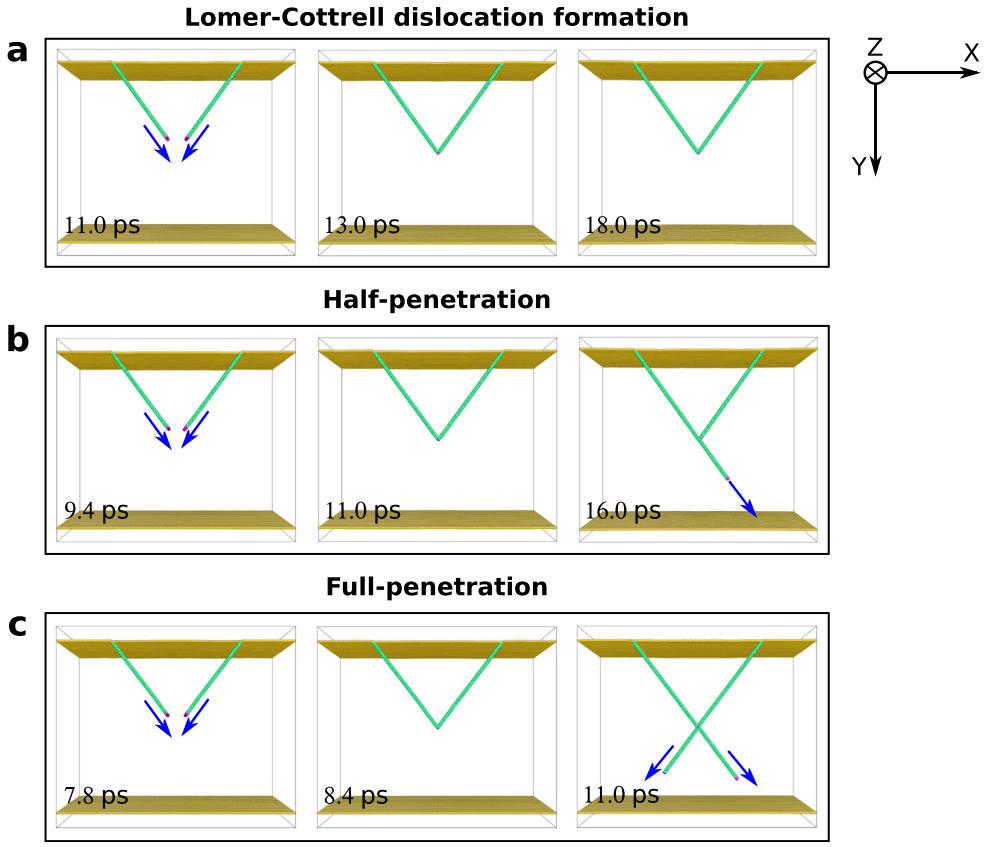

Fig. 7. Two non-coplanar partial edge dislocations experiencing Lomer-Cottrell (LC) dislocation formation and penetration, at increasing speeds. The left dislocation is denoted as dislocation 1 and the right dislocation is denoted as dislocation 2. (a) Under the axial stress of 1.0 GPa, two partial dislocations form a LC dislocation when they collide into each other at relatively low instantaneous incident speeds $v_1 \sim 0.68c_t$ and $v_2 \sim 0.62c_t$ (also see Movie 12 in Supplementary Material). (b) Under the axial stress of 1.7 GPa, half-penetration occurs with the instantaneous incident speeds $v_1 \sim 0.74c_t$ and $v_2 \sim 0.73c_t$ (also see Movie 13 in Supplementary Material). (c) Under the axial stress of 2.5 GPa, full penetration occurs with the instantaneous incident speeds $v_1 \sim 1.69c_t$ and $v_2 = 1.70c_t$ (also see Movie 14 in Supplementary Material). $c_t = 2920$ m/s is the transverse sound speed. *X*, *Y* and *Z* are along [011], $[01\bar{1}]$ and $[\bar{1}\ 00]$, respectively. Atoms on free surfaces, dislocation cores and stacking faults are rendered in yellow, magenta and green color, respectively. The short blue arrows indicate the direction of dislocation motion.

critical speed of $v_{dp} = 0.910c_t$, close to our MD simulations results (instantaneous critical speeds $v \sim 0.90c_t$ and $v \sim 0.88c_t$ right before reactions, respectively). We noticed that the rebounded partial dislocation by an extended screw dislocation also appears on a neighboring slip plane; however, only single partial rebound was observed at the critical speed, indicating biased energy partitioning onto one side of the original slip plane. Additionally, the smaller static potential energy of a partial dislocation used in the relativistic expression (compared with that of an extended dislocation, see section 3.3 for the calculation on static potential energies of partial and extended dislocations) may also contribute to the higher critical speed for surface rebound.

For a screw dislocation being fully rebounded or penetrated, the critical speed estimated from equation (5) is $0.786c_t$. However, such full rebound or penetration is rarely observed in our simulations using Cu. In order to verify this estimation, we used four different empirical potentials [24–27] for Al that allows the single full-rebound of a full screw dislocation due to the higher stacking fault energy. The critical speeds resulted from these potentials are $v \sim 0.80c_t$, $v \sim 0.80c_t$, $v \sim 0.77c_t$ and $v \sim 0.80c_t$ (all speeds are the instantaneous speeds right before the full rebound), respectively. These are again in reasonable agreement with the estimated value from equation (5).

The above discussed critical speeds are summarized in Table 1. As can be seen, all the comparisons between predicted values and MD simulation results (using different empirical potentials) show good agreement (with deviation within $0.06c_t$). It should be noted that all values in Table 1 are for reactions at low temperatures. While we showed that temperature has minor effects on the fundamental behaviors of high-speed dislocations, it does influence the critical speeds and stresses of various reactions as the dislocation speed and barrier of generating new dislocations are all functions of temperature, see Supplementary Material (through Tables S1–S4) for finite temperature effects on critical speeds of different reactions and for a brief discussion on the possible effects of phonon drag.

3.3. Quantitative verification of the relativistic expressions

Although the critical speeds predicted by equation (5) in section 3.2 have displayed good consistency with our atomistic simulation results, it is important to verify the relativistic expression quantitatively and identify its applicable range or conditions, using systematic atomistic simulations. In this section, we directly calculate the coherent kinetic energy *K* of a moving screw dislocation from large scale atomistic simulations and relate *K* to the corresponding dislocation speed to verify the relativistic expression which is based on continuum mechanics.

Before we quantitatively evaluate the coherent kinetic energy *K*, let us first quantitatively verify the assumptions made when using equation (5), i.e., a) the static potential energy of a partial dislocation is half of that for an extended dislocation with small

Table 1
Critical speeds (instantaneous speeds right before reactions) from both prediction and MD simulations for various reactions (first three reactions are surface rebound processes and the last two are penetration processes).

	Prediction	Cu [20]	Au [28]	Al [24]	Al [25]	Al [26]	Al [27]	Ni [24]
$b_f \rightarrow b_p$	$0.625c_t$	~$0.57c_t$	~$0.65c_t$	~$0.65c_t$[a]	–	~$0.64c_t$[a]	~$0.66c_t$[a]	~$0.65c_t$
$b_f \rightarrow b_f$	$0.786c_t$	–	–	~$0.80c_t$	~$0.80c_t$	~$0.77c_t$	~$0.80c_t$	–
$b_p \rightarrow 2b_p$	$0.910c_t$	~$0.90c_t$	~$0.89c_t$	–	–	~$0.88c_t$	~$0.93c_t$	~$0.90c_t$
$2b_f \rightarrow 2b_p$	$0.625c_t$	~$0.66c_t$	~$0.66c_t$	–	–	~$0.63c_t$	~$0.63c_t$[a]	~$0.61c_t$
$2b_f \rightarrow 2b_f$	$0.786c_t$	–	–	~$0.80c_t$	~$0.80c_t$	~$0.80c_t$	~$0.79c_t$	~$0.76c_t$

[a] Products that can be generated but soon annihilated due to high stacking fault energy.

dissociation width and b) the static potential energy of a partial dislocation near free surface is half of that for a partial dislocation far from free surface. In this section, we used the same dislocation length 4 nm for all atomistic configurations to ensure the reported dislocation energies are based on the same length. First the static potential energy of an extended dislocation was calculated using two atomistic configurations. The first has a dissociated screw dislocation and the second remains perfect (see Fig. S8 in Supplementary Material for details). These two atomistic configurations have similar dimensions and boundary conditions but are slightly different in the number of atoms. This is because a special periodic boundary condition was imposed along the dislocation motion direction in the first configuration when the dislocation was introduced following the method used in Ref. [53]. Thus the static potential energy of an extended dislocation was calculated by $E_0^{\text{ext}} = E_{\text{disl}} - N_{\text{disl}} \cdot E_{\text{perf}}/N_{\text{perf}}$, where E_{disl} is the total potential energy of the first configuration which has an extended dislocation, N_{disl} is the number of atoms in the first configuration, and E_{perf} and N_{perf} are those for the second configuration, respectively. Following this method, the static potential energy E_0^{ext} of a ~4 nm long extended screw dislocation was determined as 26.2 eV.

The static potential energy of a partial dislocation with respect to its distance to a free surface was then evaluated. In this set of calculations, we also used two similar atomistic configurations; one has a partial dislocation inside and the other remains perfect. However free surfaces were used in both dislocation motion direction and the slip plane normal direction. Thus both the dislocated configuration and perfect configuration have the same number of atoms. The partial dislocation length used here is also 4 nm and the potential energy of this partial dislocation is calculated according to $E_0^{\text{par}}(r) = E_{\text{disl}}(r) - E_{\text{sf}}(r) - E_{\text{perf}}$, where r is the distance of the partial dislocation from free surface, $E_{\text{disl}}(r)$ is the total potential energy of the crystal with one partial dislocation located at r, $E_{\text{sf}}(r)$ is the stacking fault energy when the partial dislocation is located at r and E_{perf} is the total potential energy of the perfect crystal. The partial dislocation was first introduced at a scaled position of 0.88 along the length between the two free surfaces. Then energy minimization was performed via the conjugate gradient method. During the energy minimization process, due to the shear stress resulted from the stacking fault energy, the introduced partial dislocation glides back to eliminate the stacking fault area and gradually approached the starting free surface with scaled position 0.00. We collected the static potential energies of this partial dislocation when it passed from 0.5 to 0.0 during the energy minimization. As shown in Fig. 8(a), the potential energy of the partial dislocation largely remains constant until it enters the sub-surface distance of ~30 nm where dramatic decrease of potential energy occurred. Fig. 8(b) shows three atomistic configurations of partial dislocations at different positions and their corresponding static potential energies. The one located in the middle of the simulation box has a potential energy of 11.4 eV. The closest partial dislocation to the free surface and the next closest partial dislocation to the free surface have potential energies 6.3 eV and 6.9 eV, respectively. As can be seen, $E_0^{\text{par}}(0.5)/E_0^{\text{par}}(\sim 0.0) = 1.81$, $E_0^{\text{ext}}/E_0^{\text{par}}(0.5) = 2.3$; these two values are very close to 2.0, thus verifying the assumptions made in using equation (5) (see the discussion in the paragraph right below equation (5)).

Next we consider the coherent kinetic K of a moving dislocation. As analyzed in section 3.2, the total kinetic energy of a system consists of the randomized incoherent kinetic energy or heat E_{incoh} and the coherent kinetic energy K due to moving dislocations. The random nature of atoms' velocities due to E_{incoh} allows one to separate out K by performing coarse graining on each velocity component of a central atom over its neighbors. Here, we obtain the coherent velocity of a given atom by averaging each of its velocity component over its neighbors with each assigned a weighting factor. The weighting factor f_i for neighbor atom i is given by $f_i = g_i/\sum_i^N g_i$, where N is the number of neighbors within the specified cutoff radius r_c and g_i is the value of Gaussian function which depends on the distance to the central atom and the standard deviation parameter δ. The proper values of r_c and δ were

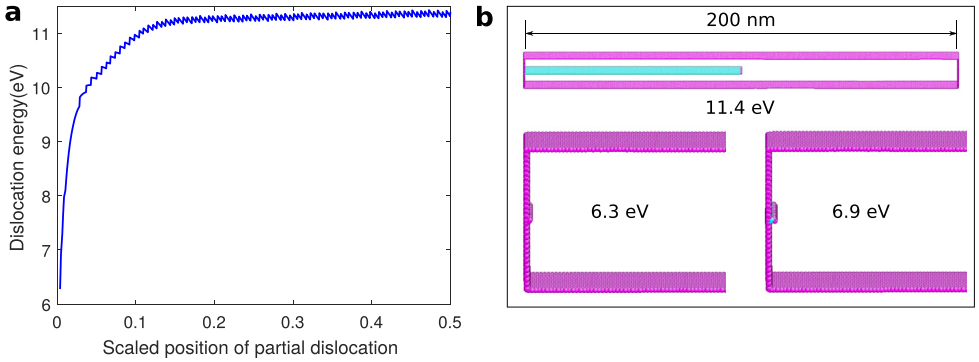

Fig. 8. Static potential energy of a partial dislocation with respect to its distance to free surface. (a) Static potential energy change vs. scaled dislocation position (0.0 represents the left free surface and 0.5 is the middle of the simulation box). (b) Three typical configurations of the partial dislocation and their corresponding static potential energies.

determined by performing the weighted averaging on a thermally equilibrated system (with temperature equals 10 K, an upper bound for temperature rise during dislocation motion at high speeds in our simulations) that has similar setups as those used for subsequent coherent kinetic energy calculation (see next paragraph for a detailed description) but without dislocation. Generally, the larger r_c and δ, the smaller the resultant kinetic energy. We tried a series of r_c and δ and found that when $r_c = 20.0$ Å and $\delta = 15$ Å, the resultant total kinetic energy of the system (a snapshot at 100 ps) reduced from 1651.8 eV (the total kinetic energy of the system) to 0.68 eV, showing that the randomized incoherent kinetic energy E_{incoh} has been effectively removed. The remnant kinetic energy after coarse graining with the same r_c and δ is even smaller for the same system but with lower temperature, e.g., it is only 0.34 eV when the system temperature is 5 K, half of that at 10 K. This small remnant kinetic energy resulted from the above choice of r_c and δ turns out to be small enough for our purpose of calculating the coherent kinetic energy as it is comparable with or much smaller than the standard deviation of the time averaged K using the same set of parameters. Therefore, we choose $r_c = 20.0$ Å and $\delta = 15$ Å for the following calculation on coherent kinetic energy.

In order to obtain the atomistic configurations with moving dislocations at steady state, here we use a simulation setup that is different from those used in previous sections. This time, periodic boundary conditions were applied in both dislocation line direction and dislocation motion direction. Free surfaces were used in the normal direction of the slip plane. The dimensions of our simulation box are 200 nm × 20 nm × 4 nm along dislocation motion direction, slip plane normal direction and dislocation line direction, respectively. Atoms in the outmost three layers of both surfaces were constrained to move in slip plane and were subjected to a Langevin thermostat at 1 K. Temperature of the rest atoms were initialized at the beginning of simulation and not controlled thereafter. An extended dislocation with screw character was introduced following the method used in Ref. [53]. The driving shear stress was applied by adding forces to atoms in the surface layers. The desired shear stress level was ramped up according to $\sigma/(1 + 6.0 \times \exp(1.0 - 0.03t))$, where σ is the desired shear stress in units of GPa and t is the simulation time in units of ps and starts from 0 ps. Based on this ramping function, the shear stress generally reaches a constant value after 300 ps. After sufficiently long time such that the overall potential energy, temperature etc. of the simulated system reach a steady state, the desired properties such as dislocation speed, core width and kinetic energy were calculated and averaged over a time period of 800 ps.

Fig. 9(a) shows the calculated K and K given by the relativistic expression with respect to dislocation speed for copper. As can be seen, K predicted by the relativistic expression is largely consistent with that obtained from MD simulations for dislocation speeds less than ~0.65c_t. Beyond this speed, K from relativistic expressions significantly deviates from the calculated values. This significant difference in K when dislocation speed is greater than ~0.65c_t is due to the onset of the so-called breathing mode of dislocations (see Fig. 9(b) for a typical example of dissociation width variation during motion with average speed of 0.79c_t), which has been demonstrated in previous research [37–39]. Thus criterion given by equation (5) should be applied with caution at very high speeds where the dissociation width variation is significant. However, we found that the relativistic expression can remain valid up to higher speed levels provided that the dislocation core width does not

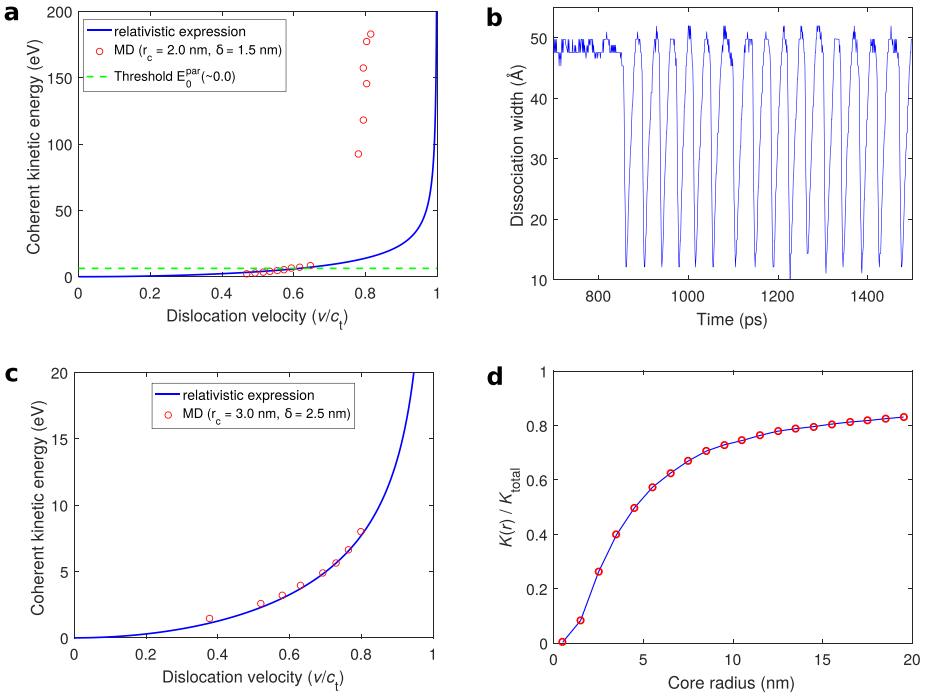

Fig. 9. Quantitative evaluation of the coherent kinetic energy for moving screw dislocations. (a) Comparison between the coherent kinetic energy obtained from MD simulations and that given by the relativistic expression. Below ~0.65c_t, results from the relativistic expression are largely consistent with that from MD simulations. Above ~0.65c_t, dislocation enters the so-called breathing mode in which the relativistic expression fails to capture the dissociation width variations and thus the prediction significantly deviates from MD simulations. Dashed line indicates the static potential energy of a partial dislocation near free surface. (b) A typical example of dissociation width variation during the breathing mode for copper. The average dislocation speed is 0.79c_t. Initially the dissociation width only has a small fluctuation (before ~850 ps). After ~850 ps, the dissociation width starts to fluctuate quasi-periodically with much larger amplitude. (c) Coherent kinetic energy for a ~4 nm long screw dislocation in Al. The static potential energy of this screw dislocation is 14.5 eV. The relativistic expression is largely consistent with MD results up to speed 0.8c_t. The dislocation core did not undergo significant width fluctuations up to 0.8c_t. (d) Normalized coherent kinetic energy of dislocation core region with respect to different core radius. Calculations were performed on a snapshot with steady speed of 0.615c_t in copper.

undergo significant changes, see Fig. 9(c) for an example of Al [24] where the dislocation core width largely remains constant up to speed ~0.8c_t. Nevertheless, the minimum critical speed for partial rebound, which is substantially below the critical speed for the breathing mode, is still correctly predicted using equation (5) (see Fig. 9(a); the intersection between the threshold energy to create a partial dislocation near free surface and the calculated/predicted K is ~0.6c_t). Fig. 9(d) shows the change of coherent kinetic energy for dislocation core region $K(r)$ with respect to different core radius r ($K(r)$ is normalized by the total coherent kinetic energy K_{total} and the calculation was performed on a snapshot taken from a simulation with steady dislocation speed 0.615c_t in copper). As can be seen, the coherent kinetic energy is highly localized; 50% of K_{total} is localized within a ~5 nm core and 80% of K_{total} is confined within a ~20 nm core.

Surface effects have been largely captured by equation (5) in the following way. On one hand, we assumed that the rebounded dislocation near free surface has a static potential energy which is half of that for a dislocation far from free surface. This assumption has been verified by our MD simulations (see Fig. 8). On the other hand, when dislocations approach free surface, the speed and coherent kinetic energy may increase due to the image force. This effect can be taken into account by using the instantaneous dislocation speed right before hitting a free surface. As shown in Fig. S9, the critical speed and coherent kinetic energy obtained from the atomistic configuration right before hitting a free surface is consistent with the prediction made by equation (5).

It should be noted that critical speed predicted by equation (5) represents the minimum speed required for an anomalous reaction (e.g., single partial rebound at free surface) because products are assumed to be static at the very moment of being created (no extra kinetic energy left to render the products relativistic and the products need to be accelerated by the applied stress). One may also add relativistic effects into the products if the reactant dislocations have extra kinetic energy and are able to directly create relativistic products. However the latter needs to be based on further studies on the detailed physics of these transient reactions.

3.4. Strongly correlated plasticity in Cu nanowire

The abnormal dislocation reactions and breeding described above may have consequences in real-world plastic deformation processes, especially those that exhibit strong correlation effects both temporally and spatially. For example, in nanometer scale

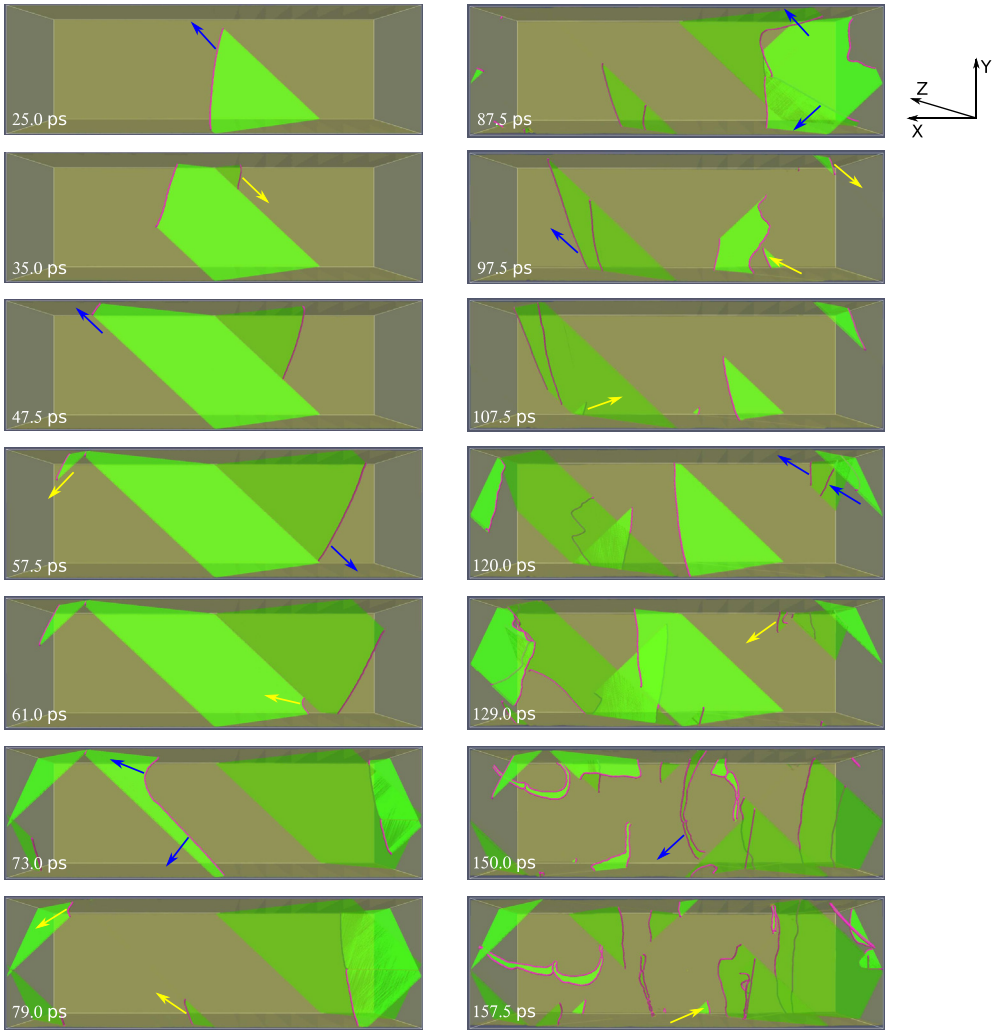

Fig. 10. Strongly correlated plasticity in Cu nanowire. The initial applied axial tensile stress is $\sigma_{xx} = 4.5$ GPa and the global strain (plastic + elastic) is kept constant as 5.7%. See Movie 15 in Supplementary Material for the sequence and details of the self-sustained multiplication that produced a high density of dislocations via rebounding and penetration events. Stacking faults, dislocation cores and free surface are rendered in green, magenta and translucent yellow, respectively. Blue arrows indicate the motion direction of incident dislocations while yellow arrows indicate the motion direction of rebounded dislocations. X, Y and Z are along [100], [010] and [001] directions, respectively.

single crystals, the specimen can be almost free of defects and approach theoretical strength. Consequently, over an acceleration distance of ~10^1 nm, the first dislocation nucleated from the surface can accelerate to ~ c_t and becomes temporarily "immortal" via the "rebound" and "penetration" mechanisms illustrated earlier, until the entire system becomes stress relaxed and the dislocation speed slows down. As discussed above, this is expected to lead to an explosive increase in the number density of dislocations that are initially strongly correlated, and hence extremely rapid shape changes.

To demonstrate such a possibility, in Fig. 10 we show a copper nanowire that was plastically relaxed via high-speed dislocations. The nanowire has a square cross-sectional area, a dimension of 95 nm × 29 nm × 29 nm, and is periodic along the X (i.e., [100]) direction. As an example, an axial stress $\sigma_{xx} = 4.5$ GPa is ramped up at the strain rate of 10^9 s^{-1}, with an initial temperature of ~1 K without any thermostats. From then on, the total strain is kept constant. A leading partial dislocation is introduced at one of the corners, after a relaxation for 10 ps at the current temperature and elastic strain. As shown in Fig. 10, the introduced leading partial quickly accelerates to a high speed and collides into the free surface (25.0 ps). At the sites where collisions occur, new dislocations are immediately generated and glide onto different slip planes (35.0 ps, 47.5 ps and 57.5 ps), leading to strongly correlated rebounding events. The rebounded dislocations continue to accelerate, penetrate other dislocations or stacking faults and collide into the free surfaces, resulting in more and more rebound events (61.0 ps–157.5 ps), in a "chain-reaction" like process. New dislocation generation is thus self-sustained, and becomes a general dislocation shower within a very short period of time, until the sample-wide stress is significantly relaxed. See Movie 15 in Supplementary Material for a detailed illustration. It is determined that surface dislocation rebound largely dominates the relaxation process though some dislocations are also nucleated from the surfaces without the help of an incident dislocation. With such processes, the elastically strained nanowire is thoroughly relaxed within hundreds of picoseconds (see Fig. S10 in Supplementary Material), exhibiting a large plasticity (transforming ~67% of the total elastic strain 5.7% into plastic strain). This is thus an example of a large strain burst due to high-speed dislocation mediated emissions that are strongly correlated both temporally and spatially [5]. We noted that such strongly correlated plasticity due to high-speed dislocations have rarely been reported in MD simulations, however, this does not necessarily mean that our results contradict previous studies. Possible reasons for failing to observe the results presented here may lie in the extremely high loading rates or very small sample sizes used in most MD simulations on nanowires. Under high strain rates, samples can be easily loaded to the athermal stress limit at which dislocation nucleation from surfaces becomes so rampant that surface rebound processes would be significantly obscured or suppressed. Here in our simulations, dislocations were "nucleated" far below the athermal stress level, which is often the case for laboratory experiments. Or if very small sample sizes such as a few nanometers in diameter were used in simulations, dislocations might not have enough acceleration length to reach high speeds, hence simple annihilation would dominate.

Supplementary video related to this article can be found at http://dx.doi.org/10.1016/j.actamat.2016.07.053.

4. Conclusions

In conclusion, we have shown that high-speed dislocations created under ultra-high stress often behave differently from conventional dislocations. The textbook-predicted dislocation annihilation (e.g. at free surface or upon encountering dislocations with opposite sign) can be defeated: instead new dislocations can be generated through "rebound", "penetration" and self-dissociation processes. These strongly correlated reactions are demonstrated here systematically via atomistic simulations. We have also confirmed that they indeed have their origin in the high kinetic energy associated with a high-speed dislocation; for the first time the criteria based on energy conservation have been analyzed and the transitions between different reaction products at various critical dislocation speeds have been rationalized and verified. The unconventional dislocation interactions with surface and other dislocations efficiently and rapidly multiply dislocations that are strongly correlated temporally and spatially [5], and can thus mediate strongly correlated plasticity in initially pristine single crystals. One possible connection to laboratory experiments is that such a strongly correlated dislocation shower, not just as an avalanche of *existing* dislocations but rather a rapid creation of a high density of *new* dislocations, may contribute to some of the unusual deformation behaviors observed at ultra-high stresses in nano-scale samples mentioned at the beginning of this article, such as the large strain bursts and shape collapse that require the instant availability of a large number of dislocations across the crystal volume.

Acknowledgement

This work was supported at JHU by the U.S. Department of Energy, Office of Science, Basic Energy Sciences, Division of Materials Sciences and Engineering, under contract no. DE-FG02-13ER46056. Q.J.L. and E.M. acknowledge the computational resources from Maryland Advanced Research Computing Center (MARCC). J.L. acknowledges support by NSF DMR-1410636 and DMR-1120901. Z.W.S. acknowledges support by NSFC 51231005 and NSFC 51321003.

Appendix A. Supplementary data

Supplementary data related to this article can be found at http://dx.doi.org/10.1016/j.actamat.2016.07.053.

References

[1] J.R. Greer, J.T.M. De Hosson, Plasticity in small-sized metallic systems: intrinsic versus extrinsic size effect, Prog. Mater. Sci. 56 (2011) 654–724.
[2] T. Zhu, J. Li, Ultra-strength materials, Prog. Mater. Sci. 55 (2010) 710–757.
[3] W.M. Mook, C. Niederberger, M. Bechelany, L. Philippe, J. Michler, Compression of freestanding gold nanostructures: from stochastic yield to predictable flow, Nanotechnology 21 (2010), 055701–055701.
[4] D. Mordehai, S.-W. Lee, B. Backes, D.J. Srolovitz, W.D. Nix, E. Rabkin, Size effect in compression of single-crystal gold microparticles, Acta Mater 59 (2011) 5202–5215.
[5] Z.-J. Wang, Z.-W. Shan, J. Li, J. Sun, E. Ma, Pristine-to-pristine regime of plastic deformation in submicron-sized single crystal gold particles, Acta Mater 60 (2012) 1368–1377.
[6] Z.-J. Wang, Q.-J. Li, Z.-W. Shan, J. Li, J. Sun, E. Ma, Sample size effects on the large strain bursts in submicron aluminum pillars, Appl. Phys. Lett. 100 (2012) 071906.
[7] W.-Z. Han, L. Huang, S. Ogata, H. Kimizuka, Z.-C. Yang, C. Weinberger, Q.-J. Li, B.-Y. Liu, X.-X. Zhang, J. Li, E. Ma, Z.-W. Shan, From "smaller is stronger" to "size-independent strength plateau": towards measuring the ideal strength of iron, Adv. Mater 27 (2015) 3385–3390.
[8] H. Bei, S. Shim, G.M. Pharr, E.P. George, Effects of pre-strain on the compressive stress-strain response of Mo-alloy single-crystal micropillars, Acta Mater 56 (2008) 4762–4770.
[9] M.B. Lowry, D. Kiener, M.M. LeBlanc, C. Chisholm, J.N. Florando, J.W. Morris Jr., A.M. Minor, Achieving the ideal strength in annealed molybdenum nanopillars, Acta Mater 58 (2010) 5160–5167.
[10] C. Chisholm, H. Bei, M.B. Lowry, J. Oh, S.A.S. Asif, O.L. Warren, Z.W. Shan, E.P. George, A.M. Minor, Dislocation starvation and exhaustion hardening in Mo alloy nanofibers, Acta Mater 60 (2012) 2258–2264.
[11] J. Weertman, High velocity dislocations, in: P.G. Shewmon, V.F. Zackay (Eds.), Response of Metals to High Velocity Deformation, Interscience, 1961, pp. p.205–247.

[12] P. Gumbsch, H. Gao, Dislocations faster than the speed of sound, Science 283 (1999) 965–968.
[13] D.L. Olmsted, L.G. Hector Jr., W.A. Curtin, R.J. Clifton, Atomistic simulations of dislocation mobility in Al, Ni and Al/Mg alloys, Modell. Simul. Mater. Sci. Eng. 13 (2005), 371–371.
[14] Z. Jin, H. Gao, P. Gumbsch, Energy radiation and limiting speeds of fast moving edge dislocations in tungsten, Phys. Rev. B 77 (2008), 094303–094303.
[15] F.C. Frank, On the equations of motion of crystal dislocations, Proc. Phys. Soc. Lond. Sect. A 62 (1949), 131–131.
[16] J.D. Eshelby, Uniformly moving dislocations, Proc. Phys. Soc. Lond. Sect. A 62 (1949), 307–307.
[17] P. Rosakis, Supersonic dislocation kinetics from an augmented peierls model, Phys. Rev. Lett. 86 (2001) 95–98.
[18] L. Pillon, C. Denoual, Y.P. Pellegrini, Equation of motion for dislocations with inertial effects, Phys. Rev. B 76 (2007) 224105.
[19] Y.-P. Pellegrini, Screw and edge dislocations with time-dependent core width: from dynamical core equations to an equation of motion, J. Mech. Phys. Solids 60 (2012) 227–249.
[20] Y. Mishin, M.J. Mehl, D.A. Papaconstantopoulos, A.F. Voter, J.D. Kress, Structural stability and lattice defects in copper: ab initio, tight-binding, and embedded-atom calculations, Phys. Rev. B 63 (2001), 224106–224106.
[21] M.A. Tschopp, D.E. Spearot, D.L. McDowell, Atomistic simulations of homogeneous dislocation nucleation in single crystal copper, Modell. Simul. Mater. Sci. Eng. 15 (2007), 693–693.
[22] T. Zhu, J. Li, A. Samanta, A. Leach, K. Gall, Temperature and strain-rate dependence of surface dislocation nucleation, Phys. Rev. Lett. 100 (2008), 025502–025502.
[23] X. Li, Y. Wei, L. Lu, K. Lu, H. Gao, Dislocation nucleation governed softening and maximum strength in nano-twinned metals, Nature 464 (2010) 877–880.
[24] Y. Mishin, D. Farkas, M.J. Mehl, D.A. Papaconstantopoulos, Interatomic potentials for monoatomic metals from experimental data and ab initio calculations, Phys. Rev. B 59 (1999) 3393–3407.
[25] F. Ercolessi, J.B. Adams, Interatomic potentials from first-principles calculations: the force-matching method, Europhys. Lett. 26 (1994), 583–583.
[26] R.R. Zope, Y. Mishin, Interatomic potentials for atomistic simulations of the Ti-Al system, Phys. Rev. B 68 (2003) 024102.
[27] L. Xiang-Yang, E. Furio, B.A. James, Aluminium interatomic potential from density functional theory calculations with improved stacking fault energy, Modell. Simul. Mater. Sci. Eng. 12 (2004) 665.
[28] H.S. Park, J.A. Zimmerman, Modeling inelasticity and failure in gold nanowires, Phys. Rev. B 72 (2005) 054106.
[29] M. Parrinello, A. Rahman, Polymorphic transitions in single crystals: a new molecular dynamics method, J. Appl. Phys. 52 (1981) 7182–7190.
[30] D. Faken, H. Jónsson, Systematic analysis of local atomic structure combined with 3D computer graphics, Comput. Mater. Sci. 2 (1994) 279–286.
[31] H. Tsuzuki, P.S. Branicio, J.P. Rino, Structural characterization of deformed crystals by analysis of common atomic neighborhood, Comput. Phys. Commun. 177 (2007) 518–523.
[32] S. Alexander, A. Karsten, Extracting dislocations and non-dislocation crystal defects from atomistic simulation data, Modell. Simul. Mater. Sci. Eng. 18 (2010) 085001.
[33] J. Li, AtomEye: an efficient atomistic configuration viewer, Modell. Simul. Mater. Sci. Eng. 11 (2003) 173.
[34] S. Plimpton, Fast parallel algorithms for short-range molecular dynamics, J. Comput. Phys. 117 (1995) 1–19.
[35] C.R. Weinberger, A.T. Jennings, K. Kang, J.R. Greer, Atomistic simulations and continuum modeling of dislocation nucleation and strength in gold nanowires, J. Mech. Phys. Solids 60 (2012) 84–103.
[36] J.R. Greer, W.C. Oliver, W.D. Nix, Size dependence of mechanical properties of gold at the micron scale in the absence of strain gradients, Acta Mater 53 (2005) 1821–1830.
[37] L. Xiong, D.L. McDowell, Y. Chen, Sub-THz Phonon drag on dislocations by coarse-grained atomistic simulations, Int. J. Plast. 55 (2014) 268–278.
[38] Z.Q. Wang, I.J. Beyerlein, Stress orientation and relativistic effects on the separation of moving screw dislocations, Phys. Rev. B 77 (2008) 184112.
[39] D. Mordehai, I. Kelson, G. Makov, Nonplanar core and dynamical behavior of screw dislocations in copper at high velocities, Phys. Rev. B 74 (2006) 184115.
[40] J.-H. Seo, Y. Yoo, N.-Y. Park, S.-W. Yoon, H. Lee, S. Han, S.-W. Lee, T.-Y. Seong, S.-C. Lee, K.-B. Lee, P.-R. Cha, H.S. Park, B. Kim, J.-P. Ahn, Superplastic deformation of defect-free Au nanowires via coherent twin propagation, Nano Lett. 11 (2011) 3499–3502.
[41] A. Sedlmayr, E. Bitzek, D.S. Gianola, G. Richter, R. Mönig, O. Kraft, Existence of two twinning-mediated plastic deformation modes in Au nanowhiskers, Acta Mater 60 (2012) 3985–3993.
[42] J.-H. Seo, H.S. Park, Y. Yoo, T.-Y. Seong, J. Li, J.-P. Ahn, B. Kim, I.-S. Choi, Origin of size dependency in coherent-twin-propagation-mediated tensile deformation of noble metal nanowires, Nano Lett. 13 (2013) 5112–5116.
[43] G. Richter, K. Hillerich, D.S. Gianola, R. Mönig, O. Kraft, C.A. Volkert, Ultrahigh strength single crystalline nanowhiskers grown by physical vapor deposition, Nano Lett. 9 (2009) 3048–3052.
[44] S. Lee, J. Im, Y. Yoo, E. Bitzek, D. Kiener, G. Richter, B. Kim, S.H. Oh, Reversible cyclic deformation mechanism of gold nanowires by twinning–detwinning transition evidenced from in situ TEM, Nat. Commun. 5 (2014).
[45] H. Zheng, A. Cao, C.R. Weinberger, J.Y. Huang, K. Du, J. Wang, Y. Ma, Y. Xia, S.X. Mao, Discrete plasticity in sub-10-nm-sized gold crystals, Nat. Commun. 1 (2010) 144.
[46] M. Sakamoto, High-velocity dislocations: effective mass, effective line tension and multiplication, Philos. Mag. A 63 (1991) 1241–1248.
[47] J. Schiøtz, K.W. Jacobsen, O.H. Nielsen, Kinematic generation of dislocations, Philos. Mag. Lett. 72 (1995) 245–250.
[48] H.J. Chu, J. Wang, I.J. Beyerlein, Anomalous reactions of a supersonic coplanar dislocation dipole: bypass or twinning? Scr. Mater. 67 (2012) 69–72.
[49] F.C. Frank, On Slip Bands as a Consequence of the Dynamic Behaviour of Dislocations. Report of 1947 Bristol Conf on Strength of Solids, 1948, pp. p.46–51.
[50] S.A. Dregia, J.P. Hirth, A rebound mechanism for Lomer dislocation formation in strained layer structures, J. Appl. Phys. 69 (1991) 2169–2175.
[51] C.H. Henager Jr., R.G. Hoagland, A rebound mechanism for misfit dislocation creation in metallic nanolayers, Scr. Mater. 50 (2004) 701–705.
[52] Y.T. Zhu, J. Narayan, J.P. Hirth, S. Mahajan, X.L. Wu, X.Z. Liao, Formation of single and multiple deformation twins in nanocrystalline fcc metals, Acta Mater 57 (2009) 3763–3770.
[53] X. Zhou, D.K. Ward, B.M. Wong, F.P. Doty, J.A. Zimmerman, Molecular dynamics studies of dislocations in CdTe crystals from a new bond order potential, J. Phys. Chem. C 116 (2012) 17563–17571.